Split Gate Photodiode based on Graphene-HgTe Heterostructure with few ns Photoresponse

Charlie Gréboval[1], Corentin Dabard[1,2], Nikita Konstantinov[3], Mariarosa Cavallo[1], Sang-Soo Chee[1], Audrey Chu[1], Tung Huu Dang[1], Adrien Khalili[1], Eva Izquierdo[1], Yoann Prado[1], Hicham Majjad[3], Xiang Zhen Xu[2], Jean-Francois Dayen[3,4*], Emmanuel Lhuillier[1*]

[1] Sorbonne Université, CNRS, Institut des NanoSciences de Paris, 4 place Jussieu, 75005 Paris, France.
[2]Laboratoire de Physique et d'Etude des Matériaux, ESPCI-Paris, PSL Research University, Sorbonne Université UPMC Univ Paris 06, CNRS, 10 rue Vauquelin 75005 Paris, France.
[3] Université de Strasbourg, IPCMS-CNRS UMR 7504, 23 Rue du Loess, 67034 Strasbourg, France
[4]Institut Universitaire de France, 1 rue Descartes, 75231 Paris cedex 05, France

Abstract: Hopping transport associated with the granular nature of nanocrystal arrays has led to the thought that nanocrystal-based devices might be incompatible with fast operations. Here we explore the design of HgTe nanocrystal-based sensors operating in the short-wave infrared and with very fast time response down to a few ns. To reach this goal, the design relies on a planar geometry to reduce the device capacitance. A strong in-built electric field is tailored via electrostatic control from two bottom split-gate electrodes, which promotes the charge extraction. While using graphene electrodes patterned over the two gate electrodes, we optimize the control on the electrostatic design of the p-n junction inside the nanocrystal array. Taking advantage of a high-k dielectric spacer, we demonstrate that the device can be operated under low gate bias (<6 V). The split-gate photodetector appears to be versatile, and can be used either in phototransistor or diode modes, upon the two gates voltages that are set to design isotype or diode-type heterojunctions. We finally highlight that time response enabled by the planar diode configuration can be made much faster than the one associated with the conventional vertical geometry.

Keywords: HgTe, nanocrystal, infrared, light detection, graphene, heterostructure, planar *p-n* junction.

*To whom correspondence should be sent: dayen@unistra.fr and el@insp.upmc.fr

INTRODUCTION

Nanocrystals (NCs) are versatile building blocks to design optoelectronic devices. In particular, the range of materials grown under colloidal nanocrystal form has been expanded, shifting their optical features from the visible to longer wavelengths, opening to NCs the market of infrared technologies (IR) where their cost effective and scalable capabilities are promising for next generations of sensors.

Naively, the polycrystalline nature of a NC thin film was considered incompatible with fast responding devices owing to hopping transport and slow carrier release resulting from trap states. This is probably why the first targeted application of infrared NCs was solar cells,[1,2] in which the device time response is not a relevant figure of merit. Nevertheless, the growing interest for low-cost alternatives to current technologies dedicated to IR sensing has pushed toward the development of new surface passivation to reduce the number of traps, while increasing the coupling between NCs. As a result, effective carrier mobilities in the order of 1 $cm^2V^{-1}s^{-1}$ have been reported,[3,4] even if even lower mobility values remain compatible with imaging applications. Such progresses on transport have enabled the integration of NCs onto read-out-circuit to design short-wave[5,6] and mid-wave[7] IR focal plane arrays. Light Detection And Ranging (LIDAR) sensing appears as another promising application for NCs, especially in the context of autonomous vehicles for which the device cost is constrained and poorly compatible with conventional technologies. In this case, operations as fast as 10 or even 100 MHz of frequencies are required for LIDAR sensors. what remains challenging and requires an updated device geometry to overcome the RC time constant limitation.[8] For PbS NCs, a time response as short as 300 ps has been obtained by reducing the pixel size to decrease the associated capacitance.[9,10] However, when a cut-off wavelength longer than 2 µm is targeted, very large PbS NCs are then required raising difficulties to obtain smooth films from particles with limited colloidal stability.[11] By contrast, for HgTe NCs[12], such fast operating diode remains mostly unreported[13–15] and currently most devices based on this material present a time response in the 100 ns to few µs range.[16–19] Further updates are required to make the device geometry compatible with GHz operation.

So far, the most popular NC sensor geometry is the vertical photodiode.[20] The intrinsic electric field is used to rectify currents or to support charge dissociation of photogenerated electron–hole pairs. However, the chemical engineering of *p-n* junctions with reliable doping profile specifications is very challenging, including difficulties such as the design of ligand generating surface dipole.[21] Moreover, the vertical stack used for photodiodes is not favorable to achieve low capacitance devices (and thus low RC time constant). As those devices are thin, their sheet capacitance, given by ε/d with ε the dielectric constant and d the thickness, turns to be large. Hence, it is highly desirable to explore alternative device concepts based on the planar geometry, which is more compatible with fast operations.

In this manuscript, we report graphene/HgTe NCs heterostructures based on a lateral device configuration to achieve NC devices with a fast photoresponse. We explore how the graphene/HgTe nanocrystals heterostructure can be used to enhance the charge dissociation through the in-built electric field resulting from *p-n* junction while the planar geometry enables low capacitance and consequently fast operation.

In order to design a planar *p-n* junction, we build our photodetector from a split-gate field-effect-transistor (FET) architecture. The latter consists of two back gates, located below the drain and source electrodes, and electrically decoupled by an Al_2O_3 dielectric thin film. The role of the gates is to enable an independent and precise control on the carrier concentration of each of the two sides of the junction that they delimitate. Taking advantage of the ambipolar properties of HgTe NCs, the two gates enable injection of electrons or holes separately in the vicinity of the two top electrodes, triggering the formation of a lateral *p-n* junction inside the NC thin film. Moreover, drain and source electrodes are made of graphene [22] Here, not only we use graphene for its gate tunable work function, but also for its large transparency to the gate induced electric field. Thanks to this

transparency, the gate effect propagates within the nanocrystal film, as opposed to a full screening of the gate induce electric field in the case of metallic electrodes. As a result, the gate induced *p-n* junction propagates within the NCs film and enhances the volume over which charge dissociation is occurring. Because our IR sensor architecture is planar, a lateral *p-n* junction, whose depletion width is directly exposed to light, is built from a simple and unique NC thin film. We demonstrate that taking advantage of the lateral space charge layer of such device, a rectification ratio of the current up to 3 decades can be achieved, together with a recorded photoresponse time on HgTe NC as short as 3 ns.

DISCUSSION

Graphene/NCs hybrid structure for photodetection has been first motivated by the large mobility of graphene.[23] In that case a graphene channel was photosensitized in the near IR by PbS NCs. By switching the NCs to HgTe, Grotevent *et al*[24] shifted the absorption of graphene in the short-wave IR, while Tang *et al*[25] even extended it to the long-wave IR. Whilst this geometry leads to large responsivities, it is also associated with two main drawbacks: a slow response induced by the transfer mechanisms of the charge carrier from the NC to the graphene, and a too large dark current resulting from the intrinsically high (dark) conductivity of graphene[26] explaining why the graphene has no longer been used as a channel, but rather as an electrode. In this case, the targeted properties are typically its optical transparency in the IR,[27,28] or its ability, as an electrode, to let back gate electric field penetrate through it to modulate the electronic states of a photosensitive material deposited on its surface.[22,28,29]

We start by fabricating a split-gate FET, as shown in Figure 1a and Figure S1-2. While such geometry is commonly used for 2D materials[26], in particular with transition metal dichalcogenides,[30,31] its use for gate NC films remains mostly unexplored. However, electrostatic doping has revealed as an efficient approach to modulate the carrier concentration of NC, using various types of gate technologies, such as dielectric,[32,33] ferroelectric,[34] ionic glass[35] and electrolyte[36]. Hence, the use of two spatially defined gates appears as a convenient approach to overcome the limited control on the intrinsic NC doping. Here, we use Al_2O_3 (40 nm) as high-k dielectric spacer on top of the two gold bottom gate electrodes, see Figure 1c and S1-2. On the top of alumina, we fabricate the drain and source electrodes from transferred graphene monolayers grown by chemical vapor deposition (CVD) (for details, see supplementary information).

The channel of the FET is made of HgTe NCs grown using the Keuleyan's procedure.[37] Absorption spectrum, in Figure 1b, shows that those particles present a cut-off energy of 0.5 eV (or ≈ 2.5 µm or ≈ 4000 cm^{-1}) and have a tripodic shape according to transmission electron microscopy[38] (background of Figure 1b). To ensure a strong interparticle coupling, the native long thiol ligands are stripped off through a concentrated ink preparation,[18] that is finally spin-coated onto the dual gated FET device. Conductive films are obtained, see Figure 1d and e. The film has an ambipolar nature, conducting both electrons and holes, with a larger hole mobility. This ambipolarity is mandatory to later induce a *p-n* junction. The temperature dependence of the current follows an Arrhenius behavior in the vicinity of room temperature. The activation energy is 160 meV, below the value of $Eg/2$≈250 meV expected for an intrinsic semiconductor, which may have been inferred by the strong p-branch observed from the FET measurements and the positioning of the neutrality point on the negative polarity side at V_N = -1.75 V.

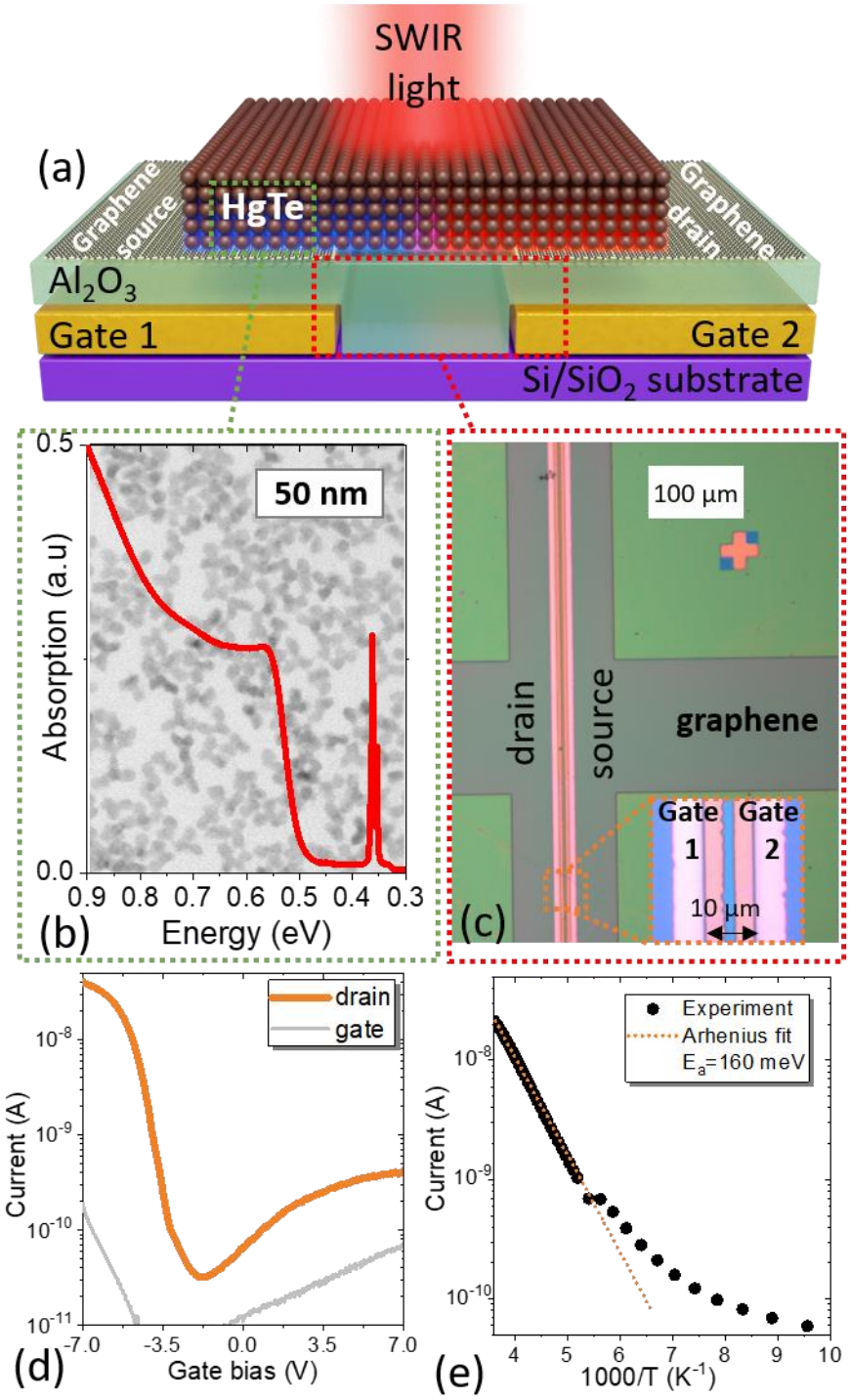

Figure 1 a. Schematic of the dual gated planar p-n graphene-HgTe heterojunction. b. Absorption spectrum of HgTe NCs with a cut-off energy of 0.5 eV (2.5 µm or 4000 cm^{-1}). Background is a transmission electron microscopy image of these NCs. c. Optical microscopy image of the dual gated device (top view) with the drain source electrode made of graphene. d. Transfer curves (drain and gate currents as a function of the applied gate bias) for a HgTe NC channel connected to the two graphene electrodes. In this case, the two gates are connected together. e. Current as a function of the temperature for a HgTe NC channel connected to the two graphene electrodes.

In Figure 2a-c, we depict the band structure of the device for different operating conditions. The graphene to HgTe band alignment (Figure 2a), in absence of applied bias, has been previously determined using photoemission[22] and revealed a small (≈0.3 eV) Schottky barrier for the holes. When the two gates are operated with the same gate bias (Figure 2b), the system behaves as a single gated FET, resulting in identical doping on both sides of the junction. In this case the I-V curve

is linear and symmetric, see Figure 2d. When the two gates are operated with opposite biases (see Figure 2c), the two sides of the junction get inversely doped with respect to each other. Such opposite polarity leads to a *p-n* junction and induces a rectifying behavior of the I-V, see Figure 2e. Gate bias will play a double role: (i) tune the Schottly barrier height at the graphene-HgTe interface and (ii) induced in the volume between the two gates (*ie* within the HgTe array) the pn junction.

In a *p-n* junction, the in-built potential V_{bi} responsible for the asymmetric I-V curve is given by: $V_{bi} = \frac{k_B T}{e} ln\left(\frac{N_D N_A}{n_i^2}\right)$ with k_B the Boltzmann constant, *T* the temperature, *e* the elementary charge, N_D (resp. N_A) the donor (resp. acceptor) dopant density and n_i the intrinsic carrier density.[39] The latter is related to the density of state through: $n_i^2 = N_C N_V exp\left(-\frac{E_G}{k_B T}\right)$. In HgTe NCs, the density of state of the conduction band N_C (resp. valence band N_V) is equal to 2ρ (resp. 6ρ), with ρ the density of NC. ρ is given by: $\rho = \frac{0.64}{4/3\pi R^3}$, where the term 0.64 relates to the NC volume fraction, assuming a random close packing, and *R* the particle radius.

The “electrostatic doping”, also referred as gate-induced charge, is a unique feature of nano-sized structures such as two-dimensional materials[40,41], nanowires[42–45] and fully depleted silicon-on insulator. In electrostatically controlled *p-n* junctions, also called split-gate geometry, on the contrary to traditional ones where donor and acceptor densities are set by implanted or chemically doped species, the values of N_D and N_A are now replaced by gate-induced electron N_* and hole P_* charge densities. If we label V_N the gate bias associated with the neutrality point of the transfer curve, $N_* = \frac{C_\Sigma |V_{G1} - V_N|}{et}$ while $P_* = \frac{C_\Sigma |V_{G2} - V_N|}{et}$ with *t* the film thickness and C_Σ the sheet capacitance, assumed to be the same for the two gates.

The asymmetry of the I-V curve appears to be strongly dependent on the operating temperature, see figure S3 and Figure 2c. At high temperatures (>200 K), the forward current is one order of magnitude larger than the reverse one, which is similar to what has been observed with metallic drain and source electrodes.[38] As the temperature is decreased, the current asymmetry drastically increases and reaches a factor 1000 at 150 K, see Figure 2f. Below this temperature, the I-V curve asymmetry drops. This drop has to be connected to the decrease of the on-current in the FET measurements, see Figure S3. This behavior relates to the thermal activation of the mobility, which magnitude reduces at low temperature.

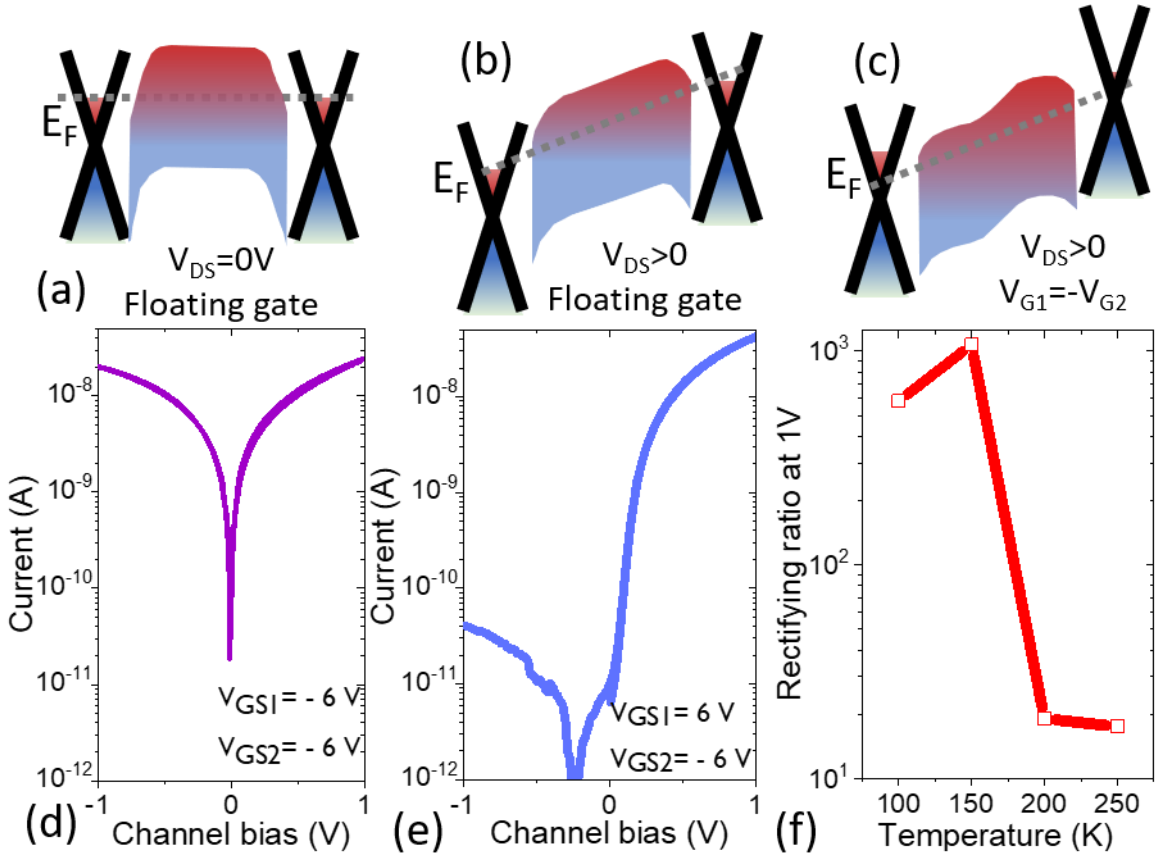

Figure 2 a. schematic of the band structure without drain or gate bias (a.), with drain bias and floating gate (b.) and with drain bias and opposite gate biases (c.). d. I-V curve at 150 K for the channel made of HgTe NCs connected to the two graphene electrodes, when the two gates are operated under strong negative bias (V_{G1}=V_{G2}=-6 V). This corresponds to the transistor regime under a strong hole injection. e. I-V curve at 150 K for the channel made of HgTe NCs connected to the two graphene electrodes, when the two gates are operated under opposite gate bias (V_{G1}=-V_{G2}=6 V) corresponding to the diode regime. f. Temperature dependence of the rectifying ratio R of the device set in the diode mode (V_{G1}=-V_{G2}=6 V), measured at 1V and defined at R= | I (+1 V) / I (-1 V) |

In the diode mode and under illumination, the device is generating photocurrent under a 0 V channel bias, see Figure 3a and b. On the contrary, in the transistor mode (*n-n* and *p-p* regimes), the photocurrent at 0 V is null and no open circuit voltage is observed, see Figure 3a. By fitting the open circuit voltage as a function of the logarithm of the incident light power, we can estimate a slope of 0.8k_BT/e, see Figure 3c. The factor 0.8 corresponds to the diode ideality factor. Values below 1 are typically associated with non-selective contact diodes.[46]

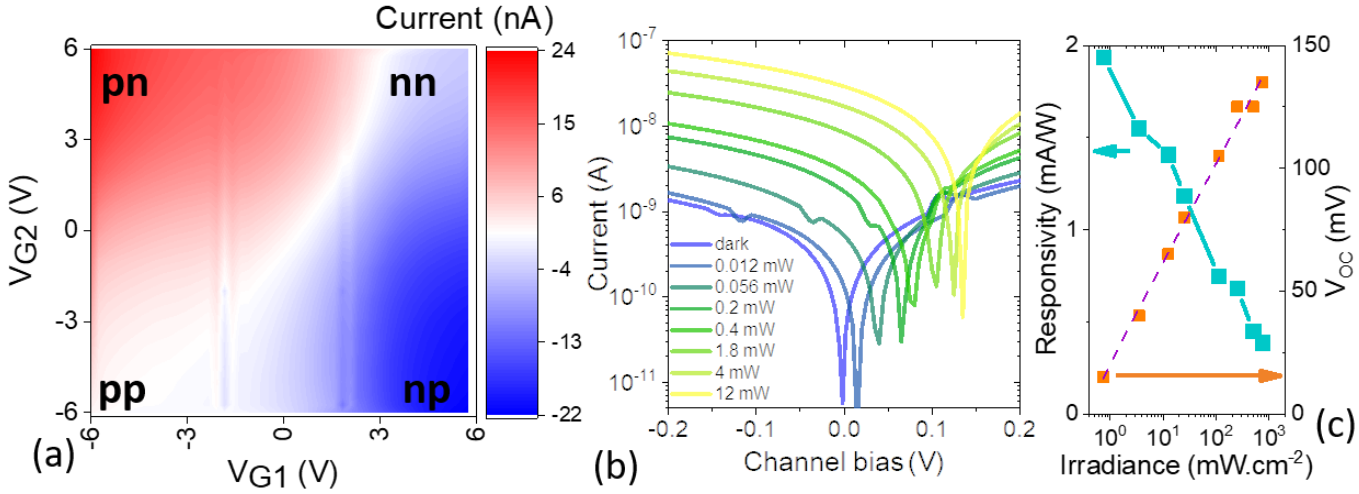

Figure 3 a. Photocurrent map, under 0 V channel bias, as a function of the applied gate biases. b. I-V curves under dark condition and under illumination by a 1.55 µm laser diode operated under various incident powers. c. Open circuit voltage (V_{OC}) and responsivity for the channel made of HgTe NCs connected to the two graphene electrodes. The purple dashed line is a log fit of the experimental data associated with a 0.8k_BT/e slope. The two gates are operated under opposite gate bias (V_{G1}=-V_{G2}=6V) corresponding to the diode regime. All measurements are made at 250 K.

We now study the photoresponse of our colloidal planar p-n photodiode. As it has been pointed out in the introduction, the time response of HgTe photodiodes were mostly reported above 100 ns, see table S1 and Figure 4a. For sake of comparison, we have built such a diode based on the following stack glass/FTO/HgTe/Hg:Ag_2Te/Au, see supporting information for details about fabrication.[19] Full decay of the vertical diode photoreponse requires almost a µs, see Figure 4a. The split-gate FET appears to be compatible with faster operations, see Figure 4a and S4. The decay time corresponding to the drop of 90% to 10% of the signal is 3 ns and correspond to a 3dB cut-off frequency of ≈110 MHz. This value matches the targeted performance required for the LIDAR operation.

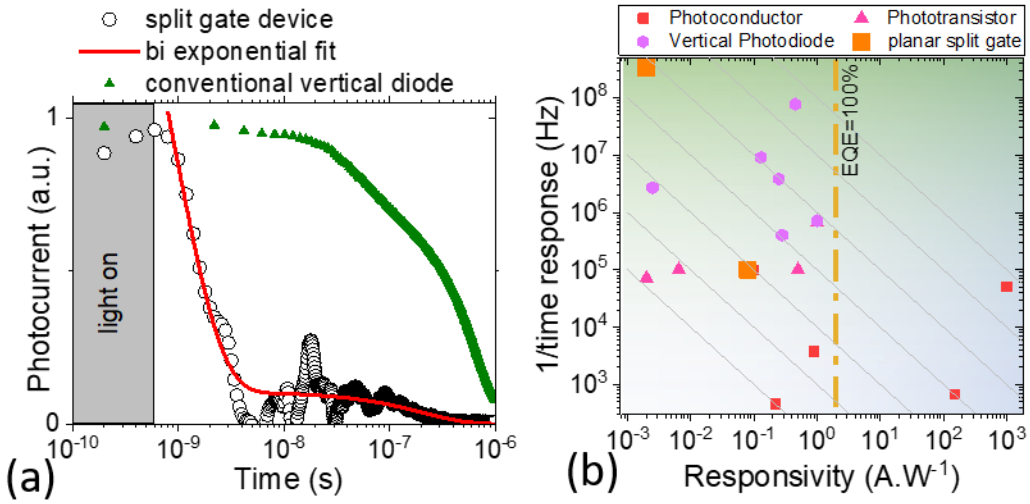

Figure 4 a. Photocurrent as a function of time after the sample gets illuminated by a 1 ns pulse at 1573 nm. The redline is a bi-exponential fit. In green we also provide the time response of a vertical geometry diode made of glass/FTO/HgTe/Hg:Ag_2Te/Au. b. Inverse of the time response as a function of the responsivity of HgTe NC-based devices operated in the SWIR based on various device geometries. Grey curves are iso gain bandwidth lines. See table S1 for associated references.

To compare the performance of this dual gate device with other devices based on the same material, we present a phase diagram where the inverse of the time response is plotted as a function of the device responsivity. In this diagram (Figure 4b), all devices mentioned in table S1 are reported. This phase diagram can be split into two main parts. Along the x axis, the responsivity corresponding to an EQE =100 % (or R=2 $A.W^{-1}$ for 2.5 µm cut-off wavelength) sets the maximal value than can be reached by diodes. Above this value, gain is required and only ultrashort devices[47] or devices based on graphene channels[24] have been reported.

It is interesting to point that most HgTe devices collected in Figure 4b are reported with time response shorter than ms, which suggests a very weak contribution of traps or at least a fast release from them. Such fast release is probably enabled by the relatively high operating temperature of HgTe NC-based SWIR devices, typically above 250 K. On Figure 4b, we also have plotted lines corresponding to iso-gain-bandwidth product (tilted grey line). The latter is defined as the ratio of

the responsivity over the time response. While the split gate device presents a modest responsivity, the achieved gain bandwidth product appears among the highest from literature.

CONCLUSION

To summarize**,** we have explored a device geometry to design a fast time photosensor from an HgTe NC array in a dual gate FET configuration. To reach this goal, we designed a low capacitance planar device in which a diode operation is induced by two bottom split-gates. The use of a high-k material makes that a p-n junction can be obtained from low bias operations (6 V typically). Graphene electrodes are used to maximize the difference of potential between the two electrodes while expanding the volume of the *p-n* junction within the NC array Thus, the combination of graphene and split-gate enables operating condition for the sensor with enhanced current modulation. The obtained time response appears to be much shorter than the obtained from conventional geometry diode and compatible with LIDAR requirement. As regards of photodiodes, future research direction includes improvement of the device light absorption, since only 10% of the incident photons are absorbed in the current configuration. Moreover, the demonstration of fine spatial electrostatic control on the carrier density profile of NC thin films goes further than photodiodes applications, and may become an ubiquitous device structure in the next generation of logic rectifiers, photovoltaics, photodetectors, and even for light emission.

METHODS

Chemicals: mercury chloride ($HgCl_2$, Strem Chemicals, 99%), **mercury salts are toxic, handle them with great care**, tellurium powder (Te, Sigma-Aldrich, 99.99%), trioctylphosphine (TOP, Alfa-Aesar, 90%), oleylamine (OLA, Acros, 80-90%), dodecanethiol (DDT, Sigma-Aldrich, 98%), mercaptoalcohol (MpOH, Merck, >99%), ethanol absolute anhydrous (VWR), methanol (Carlo Erba, 99.8%), octane (Carlo erba, 99%), toluene (Carlo Erba, 99.3%), N,N-dimethylformamide (DMF, Sigma Aldrich), Methylisobutylketone (MIBK, VWR, >98.5 %). All chemicals are used as received, except OLA that is centrifuged before being used.

1 M TOP:Te precursor: We load a 100 mL three neck flask, with 6.35 g of Te powder with 50 mL of TOP. The content of the flask is degassed, first at room temperature and once vacuum is below 1 mbar, the degassing is continued while the flask is heated at 100°C. Then the atmosphere is switched to N_2 and the temperature raised to 275 °C. The reaction is continued until the Te powder gets fully dissolved. Then the heating mantle is removed and the flaks is cooled. Once temperature is below 100 °C, the flask is degassed again. This vial is then transferred into an air free glove box and used as stock solution.

*HgTe NC growth***:** In a 100 mL three neck flask, 543 mg of $HgCl_2$ and 50 mL of oleylamine are degassed under vacuum at 110 °C. 2 mL of TOP:Te (1 M) from the stock solution are mixed with 8 mL of oleylamine. The atmosphere is switched to N_2 and the temperature cooled to 82 °C, the TOP:Te solution is quickly injected. A quenching mixture containing 9 mL of toluene and 1 mL of DDT is prepared and transferred to a 10 mL seringe. The latter is injected into the three-neck flask 2 min after the beginning of the reaction. The content of the flask is split over 4 tubes and precipitation is induced by addition of MeOH. The tubes are centrifuged and the formed pellets are redispersed in a single tube with toluene. The cleaning procedure is repeated a second time using EtOH as non-solvent. Again, the formed pellet is redispersed in toluene. The nanocrystals are then centrifuged in toluene (ie without non solvent) to get rid of the lamellar phase. The clear dark brown supernatant is transferred in a weighted tube and precipitated using methanol. The solid is dried under primary vacuum for 30 min. Nanocrystals are finally stored in toluene with a 50 $mg.mL^{-1}$ concentration.

Ag_2Te NCs growth: In a 25 mL three neck flask, 34 mg $AgNO_3$ (0.2 mM), 5 mL OLA and 0.5 mL OA are degassed at 70 °C under vacuum until the $AgNO_3$ is completely dissolved and the solution becomes clear. Under nitrogen, 0.5 mL TOP is injected into the solution. Then temperature is raised to 160 °C. At 160 °C the solution becomes orange. Now 0.1 mL TOPTe (1 M) is injected into the solution and the reaction is quenched after 10 min with a water bath. The NCs are precipitated with methanol and redispersed in chlorobenzene. At this step, 500 µL of DDT are added. The washing step is repeated one more time and finally the NCs are redispersed in hexane:octane (9:1) solution.

Material characterization: For TEM imaging, a drop of diluted NC solution is cast on a copper grid covered with an amorphous carbon film. The grid is degassed overnight under secondary vacuum. A JEOL 2010F system is operated at 200 kV for the acquisition of images. For infrared spectroscopy, we use a Fischer Nicolet iS50 system in attenuated total reflection (ATR) mode. The spectra are averaged over 32 acquisitions and have a 4 cm^{-1} resolution.

Split gate device fabrication First, gate electrodes (gap distance: 3 µm) and source/drain contact pads are patterned onto a Si/SiO_2 substrate (400 nm thick SiO_2), followed by consecutive metal deposition using a thermal evaporator given as follow: 5 nm-thick Cr, 40 nm-thick Au, and 5 nm Al (Figure S1a). This last layer is there to promote the adhesion of the subsequent alumina layer. These evaporation steps are performed while sample is under rotation to obtain soft edges. Then, we deposited 40 nm of Al_2O_3 onto devices by ALD, which serves as a gate dielectric (Figure S1b). Next, Al_2O_3 areas on contact pads of gates and source/drain are patterned, and then etched by H_3PO_4 (85%) solution at 50 ºC for 6 min, to improve contact properties (Figure S1c).
The Graphene drain and source electrodes were fabricated from monolayer graphene grown by chemical vapor deposition (CVD). We used commercially available CVD Graphene on polymer film (PMMA sacrificial layer/Graphene/Polymer stack, “Easy transfer” product, from Graphenea Inc.). The following protocol was carried out: **1**. Releasing the stack in the deionized water to detach the sacrificial layer/graphene bilayer from the bottom polymer support. **2**. Fishing the sacrificial layer/graphene by cleaned glass slides. Transferring it on the substrate previously detailed. **3**. Putting substrate on hot plate at 150°C for 2 hours in glovebox. **4**. Storing it in glovebox 24 hours. **5**. Removing the sacrificial layer into successive dipping in hot acetone (50°C,1 hour), isopropanol (1 hour), being dried by a nitrogen jet gas. Using laser lithography (Heidelberg µPG 101) and Oxygen plasma etching (Plasma Prep III) processes, electrodes spaced by 10 µm were patterned. The substrate is cleaned with acetone and rinsed with ethanol and isopropanol, before being dried by a nitrogen jet gas. AZ 1505 resist is spin-coated and annealed at 105 °C. A UV Laser setup is used to perform the litography procedure. The resist is developed in a solution of AZ 726 for 20 s, and then rinsed in DI water. A mixture of Argon and Oxygen plasmas is used to etch the exposed graphene during 120 s. The substrate is then cleaned for 1 min in acetone, before being rinsed using isopropanol and dried by a nitrogen jet gas (Figure S1d). A last step of lithography is used to connect the graphene electrode to the contact pad (Figure S1e). we deposited a Ti (10 nm)/Au (50 nm) bilayer using electron beam evaporator (Plassys MEB 550S), followed by a lift-off in acetone, and similar cleaning, rinsing and drying of the substrate as detailed previously.

*HgTe ink preparation and deposition***:** We prepare a mixture made of 15 mg of $HgCl_2$ dissolved in 9 mL of DMF, then 1 mL of mercaptoethanol is added. 500 µL of NC solution at 50 $mg.mL^{-1}$ is mixed with 5 mL of hexane. 1 mL of ligand exchange solution is added to the tube containing the NC solution and mixed. The NCs experience a phase transfer from the apolar phase to the DMF phase. The apolar phase is discarded using a pipette. 5 mL of hexane are added to perform a second cleaning. The apolar phase is again removed and another cleaning step is performed. The NCs solution in DMF is precipitated by addition of a few drops of toluene. NCs are redispersed in fresh DMF at a concentration of ≈ 160 $mg.mL^{-1}$. 15 µL of ink solution are spin-coated on the electrodes at

3000 rpm for 60 s to form a <100 nm film. To obtain thicker film, the spin-coating speed is reduced to 1200 rpm (for 120 s) and is followed by a drying step at 2500 rpm for 60 s.

Device characterization: The sample is mounted on the cold finger of a closed cycle He cryostat. Unless specified, the measurements have been conducted at 250 K under secondary vacuum. Both gates are connected to the two channels of a Keithley 2634B, while the drain source electrodes are connected to another Keithley 2634B used to apply a channel voltage and measure the resulting current. Measurements under illumination are obtained while the sample is illuminated by a 1.55 µm laser diode. The beam spot presents an aera of 1.6 mm^2. The responsivity under 0 V bias is determined from the photocurrent I-V curves.

Time – resolved measurements: For the time-resolved measurements, we use a pulsed laser (CNI laser MPL-H-1573-30µJ/pulse-1 ns pulse duration and 100 Hz repetition rate) at 1573 nm. An oscilloscope (Rohde & Schwarz, RTE 1102) acquires the outcoming signal, which is proportional to I_{DS}, through a 50 Ω resistor connected to a Femto DUPVA-70 voltage amplifier. The pulse arrival time is determined by an InGaAs photodiode used as the oscilloscope trigger.

Vertical diode fabrication: For the device fabrication, we use a FTO coated glass (ρ_s≈70-90 Ω/sq – 70 nm thickness) from Solems. The FTO electrodes are defined with optical UV lithography. The FTO-coated glass substrates were sequentially cleaned in acetone and isopropanol. The substrates were exposed to UV-ozone for 5 min. The HgTe CQD ink (is deposited onto the electrodes via spin-coating. The thickness of the film can be tuned with spin-coating speed and ink concentration. A Ag_2Te NCs layer is spin-coated, on the HgTe layer, at 2000 rpm. Then, 50 µL of $HgCl_2$ in methanol (10 mM) were dropped onto silver containing layer film and spin-dried after 15 s. the film was rinsed twice with IPA. The top layer is finally cross linked through an EDT ligand-exchange. The substrate is dipped into a 1% EDT in acetonitrile solution for 30 s and rinsed with fresh acetonitrile. A gold layer (80 nm) is deposited with thermal evaporation under secondary vacuum at the rate of 3 Å/s. To ensure an homogeneous thickness, the substrate holder was rotated during the procedure. The overlapping area between the electrodes FTO and Au defined the device area (1 mm^2).

ASSOCIATED CONTENT

Supporting information include discussion about the material synthesis, procedure for the device fabrication, additional electrical characterization and table to compare the figures of merit for state-of-the-art HgTe NC based SWIR operating light sensor.

COMPETING INTEREST

The authors declare no competing financial interests.

DATA AVAILABILITY

The data that support the findings of this study are available from the corresponding author upon reasonable request.

ACKNOWLEDGEMENTS

The project is supported by ERC starting grants blackQD (grant n° 756225). We acknowledge the use of clean-room facilities at the “Centrale de Proximité Paris-Centre”. This work has been supported by Region Ile-de-France in the framework of DIM Nano-K (grant dopQD). This work was supported by French state funds managed by the ANR within the Investissements d'Avenir programme by Labex Matisse (ANR-11-IDEX-0004-02) and Labex NIE (ANR-11-LABX-0058, and

ANR-10-IDEX-0002-02) and by grants IPER-Nano2 (ANR-18CE30-0023-01), Copin (ANR-19-CE24-0022), Frontal (ANR-19-CE09-0017), Graskop (ANR-19-CE09-0026), MIXES (ANR-19-CE09-0028), NITQuantum (ANR-20-ASTR-0008-01), Bright (ANR-21-CE24-0012-02) and MixDferro (ANR-21-CE09-0029). AC thanks Agence Innovation Defense. J.-F. D. thanks the Institut Universitaire de France (IUF) for financial support.

REFERENCES

(1) Lu, H.; Carroll, G. M.; Neale, N. R.; Beard, M. C. Infrared Quantum Dots: Progress, Challenges, and Opportunities. *ACS Nano* **2019**, *13*, 939–953.
(2) Sargent, E. H. Colloidal Quantum Dot Solar Cells. *Nature Photonics* **2012**, *6*, 133–135.
(3) Lan, X.; Chen, M.; Hudson, M. H.; Kamysbayev, V.; Wang, Y.; Guyot-Sionnest, P.; Talapin, D. V. Quantum Dot Solids Showing State-Resolved Band-like Transport. *Nature Materials* **2020**, *19*, 323–329.
(4) Chen, M.; Lan, X.; Tang, X.; Wang, Y.; Hudson, M. H.; Talapin, D. V.; Guyot-Sionnest, P. High Carrier Mobility in HgTe Quantum Dot Solids Improves Mid-IR Photodetectors. *ACS Photonics* **2019**, *6*, 2358–2365.
(5) Rauch, T.; Böberl, M.; Tedde, S. F.; Fürst, J.; Kovalenko, M. V.; Hesser, G.; Lemmer, U.; Heiss, W.; Hayden, O. Near-Infrared Imaging with Quantum-Dot-Sensitized Organic Photodiodes. *Nature Photonics* **2009**, *3*, 332–336.
(6) Chu, A.; Martinez, B.; Ferré, S.; Noguier, V.; Gréboval, C.; Livache, C.; Qu, J.; Prado, Y.; Casaretto, N.; Goubet, N.; Cruguel, H.; Dudy, L.; Silly, M. G.; Vincent, G.; Lhuillier, E. HgTe Nanocrystals for SWIR Detection and Their Integration up to the Focal Plane Array. *ACS Appl. Mater. Interfaces* **2019**, *11*, 33116–33123.
(7) Ciani, A. J.; Pimpinella, R. E.; Grein, C. H.; Guyot-Sionnest, P. Colloidal Quantum Dots for Low-Cost MWIR Imaging. In *Infrared Technology and Applications XLII*; International Society for Optics and Photonics, 2016; Vol. 9819, p 981919.
(8) Paulillo, B.; Pirotta, S.; Nong, H.; Crozat, P.; Guilet, S.; Xu, G.; Dhillon, S.; Li, L. H.; Davies, A. G.; Linfield, E. H.; Colombelli, R. Ultrafast Terahertz Detectors Based on Three-Dimensional Meta-Atoms. *Optica* **2017**, *4*, 1451–1456.
(9) Vafaie, M.; Fan, J. Z.; Morteza Najarian, A.; Ouellette, O.; Sagar, L. K.; Bertens, K.; Sun, B.; García de Arquer, F. P.; Sargent, E. H. Colloidal Quantum Dot Photodetectors with 10-ns Response Time and 80% Quantum Efficiency at 1,550 nm. *Matter* **2021**, *4*, 1042–1053.
(10) Biondi, M.; Choi, M.-J.; Wang, Z.; Wei, M.; Lee, S.; Choubisa, H.; Sagar, L. K.; Sun, B.; Baek, S.-W.; Chen, B.; Todorović, P.; Najarian, A. M.; Rasouli, A. S.; Nam, D.-H.; Vafaie, M.; Li, Y. C.; Bertens, K.; Hoogland, S.; Voznyy, O.; Arquer, F. P. G. de; Sargent, E. H. Facet-Oriented Coupling Enables Fast and Sensitive Colloidal Quantum Dot Photodetectors. *Adv. Mater.* **2021**, *33*, 2101056.
(11) Killilea, N.; Wu, M.; Sytnyk, M.; Amin, A. A. Y.; Mashkov, O.; Spiecker, E.; Heiss, W. Pushing PbS/Metal-Halide-Perovskite Core/Epitaxial-Ligand-Shell Nanocrystal Photodetectors beyond 3 μm Wavelength. *Advanced Functional Materials* **2019**, *29*, 1807964.
(12) Gréboval, C.; Chu, A.; Goubet, N.; Livache, C.; Ithurria, S.; Lhuillier, E. Mercury Chalcogenide Quantum Dots: Material Perspective for Device Integration. *Chem. Rev.* **2021**, *121*, 3627–3700.
(13) Tang, X.; Ackerman, M. M.; Shen, G.; Guyot-Sionnest, P. Towards Infrared Electronic Eyes: Flexible Colloidal Quantum Dot Photovoltaic Detectors Enhanced by Resonant Cavity. *Small* **2019**, *15*, 1804920.
(14) Livache, C.; Goubet, N.; Martinez, B.; Jagtap, A.; Qu, J.; Ithurria, S.; Silly, M. G.; Dubertret, B.; Lhuillier, E. Band Edge Dynamics and Multiexciton Generation in Narrow Band Gap HgTe Nanocrystals. *ACS Appl. Mater. Interfaces* **2018**, *10*, 11880–11887.
(15) Martinez, B.; Livache, C.; Goubet, N.; Jagtap, A.; Cruguel, H.; Ouerghi, A.; Lacaze, E.; Silly, M. G.; Lhuillier, E. Probing Charge Carrier Dynamics to Unveil the Role of Surface Ligands in HgTe Narrow Band Gap Nanocrystals. *J. Phys. Chem. C* **2018**, *122*, 859–865.
(16) Jagtap, A.; Martinez, B.; Goubet, N.; Chu, A.; Livache, C.; Gréboval, C.; Ramade, J.; Amelot, D.; Trousset, P.; Triboulin, A.; Ithurria, S.; Silly, M. G.; Dubertret, B.; Lhuillier, E. Design of a

Unipolar Barrier for a Nanocrystal-Based Short-Wave Infrared Photodiode. *ACS Photonics* **2018**, *5*, 4569–4576.
(17) Rastogi, P.; Chu, A.; Dang, T. H.; Prado, Y.; Gréboval, C.; Qu, J.; Dabard, C.; Khalili, A.; Dandeu, E.; Fix, B.; Xu, X. Z.; Ithurria, S.; Vincent, G.; Gallas, B.; Lhuillier, E. Complex Optical Index of HgTe Nanocrystal Infrared Thin Films and Its Use for Short Wave Infrared Photodiode Design. *Advanced Optical Materials* **2021**, 9, 2002066.
(18) Martinez, B.; Ramade, J.; Livache, C.; Goubet, N.; Chu, A.; Gréboval, C.; Qu, J.; Watkins, W. L.; Becerra, L.; Dandeu, E.; Fave, J. L.; Méthivier, C.; Lacaze, E.; Lhuillier, E. HgTe Nanocrystal Inks for Extended Short-Wave Infrared Detection. *Advanced Optical Materials* **2019**, *7*, 1900348.
(19) Ackerman, M. M.; Tang, X.; Guyot-Sionnest, P. Fast and Sensitive Colloidal Quantum Dot Mid-Wave Infrared Photodetectors. *ACS Nano* **2018**, *12*, 7264–7271.
(20) Chuang, C.-H. M.; Brown, P. R.; Bulović, V.; Bawendi, M. G. Improved Performance and Stability in Quantum Dot Solar Cells through Band Alignment Engineering. *Nature Materials* **2014**, *13*, 796–801.
(21) Kroupa, D. M.; Vörös, M.; Brawand, N. P.; McNichols, B. W.; Miller, E. M.; Gu, J.; Nozik, A. J.; Sellinger, A.; Galli, G.; Beard, M. C. Tuning Colloidal Quantum Dot Band Edge Positions through Solution-Phase Surface Chemistry Modification. *Nature Communications* **2017**, *8*, 15257.
(22) Noumbé, U. N.; Gréboval, C.; Livache, C.; Chu, A.; Majjad, H.; Parra López, L. E.; Mouafo, L. D. N.; Doudin, B.; Berciaud, S.; Chaste, J.; Ouerghi, A.; Lhuillier, E.; Dayen, J.-F. Reconfigurable 2D/0D p–n Graphene/HgTe Nanocrystal Heterostructure for Infrared Detection. *ACS Nano* **2020**, *14*, 4567–4576.
(23) Konstantatos, G.; Badioli, M.; Gaudreau, L.; Osmond, J.; Bernechea, M.; de Arquer, F. P. G.; Gatti, F.; Koppens, F. H. L. Hybrid Graphene–Quantum Dot Phototransistors with Ultrahigh Gain. *Nature Nanotechnology* **2012**, *7*, 363–368.
(24) Grotevent, M. J.; Hail, C. U.; Yakunin, S.; Bachmann, D.; Calame, M.; Poulikakos, D.; Kovalenko, M. V.; Shorubalko, I. Colloidal HgTe Quantum Dot/Graphene Phototransistor with a Spectral Sensitivity Beyond 3 Mm. *Advanced Science* **2021**, *8*, 2003360.
(25) Tang, X.; Lai, K. W. C. Graphene/HgTe Quantum-Dot Photodetectors with Gate-Tunable Infrared Response. *ACS Appl. Nano Mater.* **2019**, *2*, 6701–6706.
(26) Guan, X.; Yu, X.; Periyanagounder, D.; Benzigar, M. R.; Huang, J.-K.; Lin, C.-H.; Kim, J.; Singh, S.; Hu, L.; Liu, G.; Li, D.; He, J.-H.; Yan, F.; Wang, Q. J.; Wu, T. Recent Progress in Short- to Long-Wave Infrared Photodetection Using 2D Materials and Heterostructures. *Advanced Optical Materials* **2021**, *9*, 2001708.
(27) Tang, X.; Chen, M.; Kamath, A.; Ackerman, M. M.; Guyot-Sionnest, P. Colloidal Quantum-Dots/Graphene/Silicon Dual-Channel Detection of Visible Light and Short-Wave Infrared. *ACS Photonics* **2020**, *7*, 1117–1121.
(28) Gréboval, C.; Noumbé, U. N.; Chu, A.; Prado, Y.; Khalili, A.; Dabard, C.; Dang, T. H.; Colis, S.; Chaste, J.; Ouerghi, A.; Dayen, J.-F.; Lhuillier, E. Gate Tunable Vertical Geometry Phototransistor Based on Infrared HgTe Nanocrystals. *Appl. Phys. Lett.* **2020**, *117*, 251104.
(29) Konstantinov, N.; Tauzin, A.; Noumbé, U. N.; Dragoe, D.; Kundys, B.; Majjad, H.; Brosseau, A.; Lenertz, M.; Singh, A.; Berciaud, S.; Boillot, M.-L.; Doudin, B.; Mallah, T.; Dayen, J.-F. Electrical Read-out of Light-Induced Spin Transition in Thin Film Spin Crossover/Graphene Heterostructures. *J. Mater. Chem. C* **1399**, *9*, 2712–2720.
(30) Molina-Mendoza, A. J.; Paur, M.; Mueller, T. Nonvolatile Programmable WSe_2 Photodetector. *Advanced Optical Materials* **2020**, *8*, 2000417.
(31) Groenendijk, D. J.; Buscema, M.; Steele, G. A.; Michaelis de Vasconcellos, S.; Bratschitsch, R.; van der Zant, H. S. J.; Castellanos-Gomez, A. Photovoltaic and Photothermoelectric Effect in a Double-Gated WSe_2 Device. *Nano Lett.* **2014**, *14*, 5846–5852.
(32) Lhuillier, E.; Keuleyan, S.; Zolotavin, P.; Guyot-Sionnest, P. Mid-Infrared HgTe/As_2S_3 Field Effect Transistors and Photodetectors. *Advanced Materials* **2013**, *25*, 137–141.
(33) Chen, M.; Lu, H.; Abdelazim, N. M.; Zhu, Y.; Wang, Z.; Ren, W.; Kershaw, S. V.; Rogach, A. L.; Zhao, N. Mercury Telluride Quantum Dot Based Phototransistor Enabling High-Sensitivity Room-Temperature Photodetection at 2000 nm. *ACS Nano* **2017**, *11*, 5614–5622.

(34) Gréboval, C.; Chu, A.; Magalhaes, D. V.; Ramade, J.; Qu, J.; Rastogi, P.; Khalili, A.; Chee, S.-S.; Aubin, H.; Vincent, G.; Bals, S.; Delerue, C.; Lhuillier, E. Ferroelectric Gating of Narrow Band-Gap Nanocrystal Arrays with Enhanced Light–Matter Coupling. *ACS Photonics* **2021**, *8*, 259–268.
(35) Gréboval, C.; Noumbe, U.; Goubet, N.; Livache, C.; Ramade, J.; Qu, J.; Chu, A.; Martinez, B.; Prado, Y.; Ithurria, S.; Ouerghi, A.; Aubin, H.; Dayen, J.-F.; Lhuillier, E. Field-Effect Transistor and Photo-Transistor of Narrow-Band-Gap Nanocrystal Arrays Using Ionic Glasses. *Nano Lett.* **2019**, *19*, 3981–3986.
(36) Livache, C.; Izquierdo, E.; Martinez, B.; Dufour, M.; Pierucci, D.; Keuleyan, S.; Cruguel, H.; Becerra, L.; Fave, J. L.; Aubin, H.; Ouerghi, A.; Lacaze, E.; Silly, M. G.; Dubertret, B.; Ithurria, S.; Lhuillier, E. Charge Dynamics and Optolectronic Properties in HgTe Colloidal Quantum Wells. *Nano Lett.* **2017**, *17*, 4067–4074.
(37) Keuleyan, S.; Lhuillier, E.; Guyot-Sionnest, P. Synthesis of Colloidal HgTe Quantum Dots for Narrow Mid-IR Emission and Detection. *J. Am. Chem. Soc.* **2011**, *133*, 16422–16424.
(38) Chee, S.-S.; Gréboval, C.; Magalhaes, D. V.; Ramade, J.; Chu, A.; Qu, J.; Rastogi, P.; Khalili, A.; Dang, T. H.; Dabard, C.; Prado, Y.; Patriarche, G.; Chaste, J.; Rosticher, M.; Bals, S.; Delerue, C.; Lhuillier, E. Correlating Structure and Detection Properties in HgTe Nanocrystal Films. *Nano Lett.* **2021**, 21, asap.
(39) Sze, S. M.; Kwok, K. N. *Physics of Semiconductor Devices*; John Wiley & Sons, Ltd, 2006.
(40) Williams, J. R.; DiCarlo, L.; Marcus, C. M. Quantum Hall Effect in a Gate-Controlled *p-n* Junction of Graphene. *Science* **2007**, *317*, 638–641.
(41) Beck, M. E.; Hersam, M. C. Emerging Opportunities for Electrostatic Control in Atomically Thin Devices. *ACS Nano* **2020**, *14*, 6498–6518.
(42) Heinzig, A.; Slesazeck, S.; Kreupl, F.; Mikolajick, T.; Weber, W. M. Reconfigurable Silicon Nanowire Transistors. *Nano Lett.* **2012**, *12*, 119–124.
(43) Lee, J. U.; Gipp, P. P.; Heller, C. M. Carbon Nanotube P-n Junction Diodes. *Appl. Phys. Lett.* **2004**, *85*, 145–147.
(44) Appenzeller, J.; Lin, Y.-M.; Knoch, J.; Avouris, Ph. Band-to-Band Tunneling in Carbon Nanotube Field-Effect Transistors. *Phys. Rev. Lett.* **2004**, *93*, 196805.
(45) Fossum, J. G.; Trivedi, V. P. *Fundamentals of Ultra-Thin-Body MOSFETs and FinFETs*; 1st ed, Cambridge University Press: Cambridge, 2013. DOI: 10.1017/CBO9781139343466
(46) Tress, W.; Yavari, M.; Domanski, K.; Yadav, P.; Niesen, B.; Baena, J. P. C.; Hagfeldt, A.; Graetzel, M. Interpretation and Evolution of Open-Circuit Voltage, Recombination, Ideality Factor and Subgap Defect States during Reversible Light-Soaking and Irreversible Degradation of Perovskite Solar Cells. *Energy Environ. Sci.* **2018**, *11*, 151–165.
(47) Chu, A.; Gréboval, C.; Prado, Y.; Majjad, H.; Delerue, C.; Dayen, J.-F.; Vincent, G.; Lhuillier, E. Infrared Photoconduction at the Diffusion Length Limit in HgTe Nanocrystal Arrays. *Nature Communications* **2021**, *12*, 1794.

TOC graphic

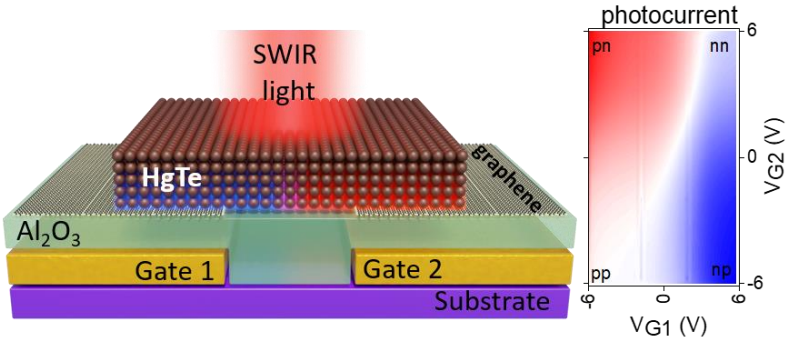
SWIR
light
HgTe
graphene
Al_2O_3
Gate 1
Gate 2
Substrate
photocurrent
pn
nn
pp
np
6
0
-6
V_{G2} (V)
V_{G1} (V)